Modeling of chromium precipitation in Fe-Cr alloys

J. Wallenius,[1,2] P. Olsson,[2] C. Lagerstedt,[1] N. Sandberg,[1] R. Chakarova,[1] and V. Pontikis[3]
[1]*Department of Nuclear and Reactor Physics, Royal Institute of Technology, Stockholm, Sweden*
[2]*Department of Neutron Research, Uppsala University, Uppsala, Sweden*
[3]*CNRS-CECM, Paris, France*
(Received 4 November 2003; published 5 March 2004)

We have implemented a set of Embedded Atom Method (EAM) potentials for simulation of Fe-Cr alloys. The functions for the pure elements were fitted to the respective elastic constants, vacancy formation energy, and thermal expansion coefficients. For Cr, properties of the paramagnetic state were applied, providing a positive Cauchy pressure and hence applicability of the EAM. By relaxing the requirement of reproducing the pressure–volume relation at short interaction distances, stability of the $\langle 110 \rangle$ self-interstitial could be obtained. Our Fe-potential gives $E^f_{\langle 110 \rangle} - E^f_{\langle 111 \rangle} = -0.23$ eV. Mixed Fe-Cr pair potentials were fitted to the calculated mixing enthalpy of ferromagnetic Fe-Cr, which is negative for Cr concentrations below 6%. Simulation of thermal aging in Fe-Cr alloys using a potential fitted to the mixing enthalpy of Fe-20Cr exhibited pronounced Cr-precipitation for temperatures below 900 K, in agreement with the phase diagram. No such ordering was observed at any temperature using a potential fitted to the mixing enthalpy of Fe-5Cr. Applied to recoil cascade simulations the new potentials predict a smaller number of surviving defects than potentials found in the literature. We obtain a cascade efficiency of 0.135 NRT for damage energies inbetween 10 and 20 keV. An enhanced probability for Cr atoms to end up in defect structures is observed.

DOI: 10.1103/PhysRevB.69.094103 PACS number(s): 61.66.Dk, 61.80.Hg, 61.82.Bg

I. INTRODUCTION

An improved understanding of the radiation effects in ferritic steels is of importance for development of new reactors and maintenance of already operating systems. Neutron and proton irradiation cause hardening, embrittlement, and dimensional instability of the construction components. The material response is complicated with a strong dependence on the particular composition. Experiments on irradiation of Fe-Cr alloys at doses below 15 DPA, where impact of He generation is possible to neglect, show that adding 2%–6% of Cr leads to a decrease in swelling as compared to pure Fe.[1,2] There is a general trend towards a minimum in ductile to brittle transition temperatures at about nine percent Cr content. Formation of the Cr rich α' phase above Cr concentrations of 10% is a major cause of hardening, indicating that chromium plays a main role in the qualitative understanding of Fe-Cr properties in- and out of pile.[3–7]

The Molecular Dynamics (MD) method is widely used as a basic theoretical tool, providing physical insight into kinetic processes and interactions leading to the formation of defect clusters, dislocation loops, etc. The validity of the conclusions is directly related to the validity of the interaction potential adopted. A binary alloy potential is usually constructed on the basis of the potentials of the elements constituting the alloy.[8,9] Thus the quality of the potential is determined by the extent to which the pure element, and the alloy properties, are reproduced.

Two different types of many-body potentials have been used in MD studies of bcc-iron reported in the literature, namely Finnis-Sinclair potentials, relying on a second moment approximation to the tight binding theory,[10–12] and Embedded Atom Method (EAM) potentials,[13–18] having their roots in Density Functional Theory.

Fe-Cr alloy potentials have also been constructed using the Finnis-Sinclair approach[19] as well as the EAM.[20] These are fitted to measurements of mixing enthalpy and to the lattice parameter of the alloy. The experimental values of the heat of mixing used in those works are however valid only for the paramagnetic state of the material (above the Curie temperature). Further, properties of antiferromagnetic (AFM) Cr were used in fitting of the Cr potential used by these authors, in spite of the negative Cauchy pressure of the AFM state.

The objective of the present work is to construct a set of Fe-Cr potentials that can reproduce essential properties of the alloy, such as the mixing enthalpy of the ferromagnetic (FM) state. The potentials should be applicable to simulations of the primary defect formation induced by high energy recoils, as well as to modeling of the subsequent defect evolution. It has to be noted that experimental data describing basic Fe-Cr alloy characteristics of use to the potential fitting, are not always available. In our case, there are experimental data for the bulk modulus of Fe-Cr alloys with different Cr contents. However, no measurements are reported for the mixing enthalpy of ferromagnetic Fe-Cr. Therefore, our modeling approach integrates *ab initio* calculations of Fe-Cr alloy properties, design of an EAM potential fitted to these data, and usage of the potential in MD cascade simulations.

In what follows, we will describe our approach to obtain physically consistent EAM-potentials for ferromagnetic iron, paramagnetic (PM) chromium, and ferromagnetic alloys of these elements. The applicability of our potentials is corroborated by kinetic Monte Carlo simulation of thermal ageing of alloys with varying concentrations of chromium. We then account for results from recoil cascade calculations, pointing out significant differences in defect production in the alloy, as compared to pure iron. Finally we discuss the impact of our results on the general understanding of Fe-Cr properties in- and out of pile.

 ©2004 The American Physical Society

II. CONSTRUCTION OF THE EAM POTENTIAL

Within the EAM formalism, the total energy of the system of n atoms is written as a sum over atomic energies,[13]

$$E_{\mathrm{tot}}=\sum_{i=1}^{n} E_i=\sum_{i=1}^{n}\left[\frac{1}{2}\sum_{j=1}^{n}\Phi(r_{ij})+F(\rho_i)\right], \tag{1}$$

where $\Phi(r_{ij})$ is the pairwise (electrostatic) interaction between atoms i and j; the function $\rho_i=\Sigma_{j\neq i}\rho(r_{ij})$ represents the electron density of the host system with atom i removed and r_{ij} is the scalar distance between atoms i and j. $F(\rho_i)$ is the many body term, i.e., the quantum mechanical energy required to embed atom i into a homogeneous electron gas of density ρ_i. Because the electron density depends only on scalar distances to neighboring atoms, the many body term here has no angular dependence. The curvature of F may be interpreted in terms of the traditional chemical bonding concept, where a new bond increases the total bonding energy but decreases the average energy per bond. In this context, ρ_i becomes a measure of the total bond order and $\rho(r)$ is a bond sensor. The weakening of successive bonds corresponds to a positive curvature of F,

$$\frac{\partial^2 F}{\partial \rho^2}>0. \tag{2}$$

The complete EAM energy expression in the case of binary Fe-Cr alloys involves definitions for the pair potentials $\Phi_{\mathrm{Fe}}(r),\Phi_{\mathrm{Cr}}(r)$ of pure Fe and Cr, the mixed pair potential $\Phi_{\mathrm{FeCr}}(r)$, the electronic density functions $\rho_{\mathrm{Fe}}(r),\rho_{\mathrm{Cr}}(r)$ and the embedding functions $F_{\mathrm{Fe}}(\rho)$ and $F_{\mathrm{Cr}}(\rho)$,

$$\begin{aligned}E_{\mathrm{tot}}=&\sum_{i_{\mathrm{Fe}}} F_{\mathrm{Fe}}(\rho_i)+\sum_{i_{\mathrm{Cr}}} F_{\mathrm{Cr}}(\rho_i)+\frac{1}{2}\sum_{i_{\mathrm{Fe}},j_{\mathrm{Fe}}}\Phi_{\mathrm{Fe}}(r_{ij})\\&+\frac{1}{2}\sum_{i_{\mathrm{Fe}},j_{\mathrm{Cr}}}\Phi_{\mathrm{FeCr}}(r_{ij})+\frac{1}{2}\sum_{i_{\mathrm{Cr}},j_{\mathrm{Cr}}}\Phi_{\mathrm{Cr}}(r_{ij})\\&+\frac{1}{2}\sum_{i_{\mathrm{Cr}},j_{\mathrm{Fe}}}\Phi_{\mathrm{FeCr}}(r_{ij}).\end{aligned} \tag{3}$$

It is seen from Eq. (3) that the potentials of the pure elements potentials are part of the alloy potential.

The following parametric form of the pair interaction terms is assumed:[12,15]

$$\Phi(r)=\sum_{i=1}^{5} a_i(r-r_i)^3 H(r_i-r). \tag{4}$$

Here, r_i are knot points of the cubic splines used to represent the potential, H is the Heaviside step function, and a_i are spline coefficients. The atom electron density is approximated by the Thomas-Fermi screening function suggested in Ref. 15.

The Fe and Cr embedding functions are calculated by fitting the cohesive energy to the Rose expression, which gives the equation of state of a perfect crystal as a function of the reduced lattice parameter $\bar{a}$,[21]

$$E_{\mathrm{Rose}}(\bar{a})=-E_{\mathrm{coh}}(1+\bar{a})e^{-\bar{a}} \tag{5}$$

with

$$\bar{a}=\sqrt{\frac{9\Omega B}{E_{\mathrm{coh}}}}\left(\frac{R_1}{R_{1e}}-1\right), \tag{6}$$

where R_{1e} is the equilibrium value of the distance to the nearest neighbor. Ω is the atomic volume and B denotes the bulk modulus. Note that the alloy bulk modulus is not involved in expression (6), but only the bulk modulus of the pure elements. Since the range of the interactions needs to be finite, a cut-off is introduced in the electron density, with a corresponding modification of the Rose expression for large lattice parameters.[9,22]

A. Potentials for Fe and Cr

The fitting procedure has been performed in several steps. Three of the spline coefficients for ferromagnetic iron, corresponding to knot points larger than R_{1e}, were obtained by fitting to the lattice parameter, cohesive energy, vacancy formation energy, and elastic constants as measured at 0 K. A modified version of the MERLIN code package was written for this step of the procedure. The package is based on elastic theory of deformation, including multiparametric optimization with options for different algorithms.[23,24] The conditions of equilibrium are expressed as a requirement of no stresses in a perfect crystal. Stresses are evaluated by expanding the energy to the first order with respect to an infinitesimal homogeneous strain applied to the system. The second order elastic constants are evaluated by expanding the energy of the system to the second order with respect to an infinitesimal homogeneous stress. For example,

$$C_{44}=\frac{\partial^2 E_{\mathrm{tot}}}{\partial \gamma^2} \tag{7}$$

with γ being the angle of distortion by shear deformation imposed on the crystal when keeping the volume constant. In the case of compression in one direction and expansion in the other, the amplitude of deformation for a constant volume is denoted by ϵ, and the corresponding elastic constant is

$$C'=\frac{1}{2}(C_{11}-C_{12})=\frac{1}{4}\frac{\partial^2 E_{\mathrm{tot}}}{\partial \epsilon^2}. \tag{8}$$

The bulk modulus is obtained by simulating isotropic compression,

$$B=\frac{1}{9}\frac{\partial^2 E_{\mathrm{tot}}}{\partial \epsilon^2}. \tag{9}$$

The embedding function of iron was then calculated using these three spline coefficients for the pair potential. After thus fixing the embedding function, the fourth spline coefficient was determined by fitting to the lattice parameter of iron at room temperature. The position of the corresponding knot point was adjusted to mimic the temperature depen-

TABLE I. Knot points and spline coefficients for the pair potentials of Fe and Cr obtained in the present work. The knot points are given in units of nearest neighbor distance.

	Fe	(a_0=0.2860 nm)	Cr	(a_0=0.2875 nm)
i	r_i	a_i	r_i	a_i
1	0.945	2633	0.945	310
2	0.967	−2500	0.972	−603
3	1.030	10.75857	1.150	50.28020
4	1.320	−24.28842	1.280	−61.24700
5	1.540	7.078864	1.470	14.66964

dence of the thermal expansion coefficient in the temperature range 0–600 K. The molecular dynamics code XMD was used for this purpose, in which the condition of constant pressure is imposed by the *pressure clamp* command.[25] The final spline coefficient was set to ensure a smooth transition of the pair potential into the universal screened Coulomb function of Biersack *et al.*[11,12,26]

A similar procedure was implemented to obtain the potential for pure chromium. Previous attempts to fit a central many-body potential to the elastic constants of antiferromagnetic chromium have failed, as may be expected from the negative value of the Cauchy pressure at 0 K,

$$\frac{1}{2}(C_{12}-C_{44}) \simeq -13 \text{ GPa}. \tag{10}$$

We note however, that at temperatures relevant for reactor operation ($T>450$ K), chromium is paramagnetic, featuring a positive Cauchy pressure.[27] Further, it is sufficient to add a few percent of iron or vanadium to obtain an alloy that is paramagnetic at room temperature.[28,29] We therefore fit our Cr potential to the elastic constants of paramagnetic chromium, linearly extrapolated down to 0 K. Stiffening of the pair potential is made by fitting to thermal expansion coefficients measured for paramagnetic Cr–5V, being equal to the expansion coefficient of pure Cr when $T>600$ K.[29] Considering that the Cr precipitates observed in real Fe-Cr alloys contain about 15% iron, we believe that our potential for paramagnetic Cr should be valid for describing Cr–Cr interactions in the present context.

In Table I we list the resulting spline coefficients and knot points for Fe and Cr. In Fig. 1 the pair-potentials are plotted as function of r. Note the slightly larger depth of the potential for paramagnetic Cr, reflecting the larger vacancy formation energy predicted for Cr.

We note that by stiffening the pair potentials inside the equilibrium nearest neighbor distance, *after having fixed* the embedding function, we violate the pressure–volume relation given by the Rose expression (5). The reason for doing so, is that we otherwise were unable to simultaneously fit experimental values for $E_{\text{bcc}}-E_{\text{fcc}}$, $E^f_{\langle 110\rangle}-E^f_{\langle 111\rangle}$ and the thermal expansion coefficient. Our potentials are hence not applicable to simulation of isotropic compression under high pressure. However, the presence of high electron densities in recoil cascades as well as in defect configurations are of local character, which may be difficult to characterize through an equation of state like the Rose expression.

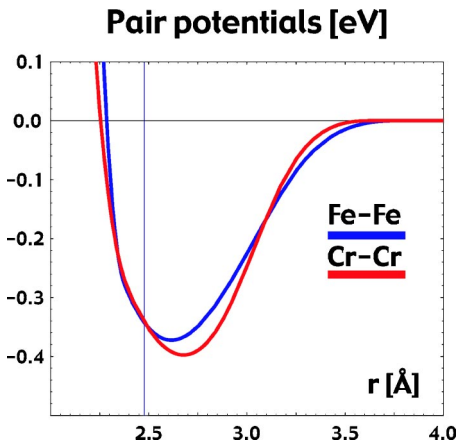

FIG. 1. (Color online) Pair potentials for ferromagnetic Fe (blue line) and paramagnetic Cr (red line) obtained in the present work.

B. Mixed Fe-Cr pair potentials

The potentials obtained for the pure elements have been further used in Eq. (3) to calculate the parameters a_i for the mixed Fe-Cr pair potential, fitting them to the mixing enthalpy of the ferromagnetic alloy. Table II displays the formation energy of ferromagnetic Fe-Cr calculated with the EMTO method.[31]

Previous attempts to construct mixed pair potentials for Fe-Cr (Refs. 18,20) relied on fitting to the formation energy of the paramagnetic state of the alloy, which is strictly positive. A single pair-potential for the Fe-Cr interaction would however not be able to reproduce the change in sign of the formation energy of the relevant magnetic state. Therefore, a set of potentials have to be created, providing the correct total energy of the random ferromagnetic alloy. In the present paper, we have performed the fitting for Cr-concentrations of 5% and 20%. The lower concentration should yield a potential with small but negative mixing enthalpy, thus ensuring phase stability at all temperatures. The larger concentration was selected to study a region where the predicted mixing enthalpy is positive, and Cr precipitation (formation of the α' phase) is observed in real materials.[3,5]

TABLE II. Formation energies ΔH_f of random ferromagnetic Fe-Cr alloys, calculated with the Exact Muffin Tin Orbital *Ab Initio* method (Ref. 31).

Cr-fraction	ΔH_f (meV)
0.02	−1.8
0.04	−1.3
0.06	+0.6
0.08	+5.1
0.10	+10.4
0.15	+27.9
0.20	+45.3

TABLE III. Knot points and spline coefficients for the mixed Fe-Cr pair potentials obtained in the present work. The knot points are given in units of nearest neighbor distance.

	Fe-5Cr	($a_0=0.2861$ nm)	Fe-20Cr	($a_0=0.2863$ nm)
i	r_i	a_i	r_i	a_i
1	0.945	2239	0.945	2624
2	0.967	−2199	0.967	−2476
3	1.030	0.000	1.030	10.000
4	1.400	−12.737	1.320	−24.500
5	1.650	4.210	1.53	7.620

The parameters obtained for the Fe-Cr mixed pair potentials are given in Table III. The sharp dip in the measured bulk modulus at Cr concentrations about 5% (Ref. 30) lead us to assume a longer range for the corresponding pair potential. Due to the lack of thermal expansion data for the alloy, stiffening of the potentials at short distances was made in a rather arbitrary fashion, simply requiring a smooth transition to the universal Coulomb screening function at $r \simeq 1.7$ Å.

III. VERIFICATION OF THE POTENTIALS

The quality of the potential has been inspected by calculations of elastic constants, structural stability, and formation energies of various defect configurations. The results are shown in Tables IV, V and VII. Comparing with experimental data and values obtained by other authors, one may note the following: The potential here presented reproduces more closely the experimental elastic characteristics and structural stability of pure iron than the EAM-potentials published by Simonelli *et al.*. Our relaxed vacancy formation energy (2.04 eV) was fitted to the resistivity measurements by De Schepper *et al.*,[34] indicating a significantly higher value for E^f_{vac} than earlier measurements in less pure materials.[40] The potential *predicts* an activation energy for self-diffusion equal to 2.91 eV, in very good agreement with data obtained at temperatures sufficiently low for the influence of paramagnetism to be safely neglected.[35,36]

Our fit to thermal expansion data was made using a single spline coefficient, and can thus not be expected to reproduce measured data over the whole temperature range. One may note however that potentials not fitted to thermal expansion underestimates the expansion by a factor of 2 or more.

In comparison with the Finnis-Sinclair potential developed by Ackland and co-workers, our potential yields a stability of the $\langle 110\rangle$ interstitial with respect to the $\langle 111\rangle$ configuration that is in better agreement with measured data. The predicted absolute formation energy of the Fe self-interstitial is higher than what results from using any other potential found in literature. We note that the experimental values are derived from measurements of stored energy release per resistivity recovery ($dQ/d\rho$) in samples irradiated at low temperature.[38–41] The enthalpy for formation of a Frenkel pair is obtained by multiplying $dQ/d\rho$ with an assumed resistivity ρ_F for a single Frenkel pair. Estimates of ρ_F vary from 0.20 to 0.30 m$\Omega\times$cm.[42,43] Selecting the higher value,

TABLE IV. Properties of pure iron obtained with the potential for ferromagnetic Fe here presented. Elastic constants are given in units of GPa, energies in eV, and thermal expansion coefficients in units of 10^{-6}. Comparison is made with experimental data and values calculated using the potentials of Simonelli (Ref. 15) and Ackland (Ref. 12).

Fe property	This work	Expt.	Sim A	Sim B	Ackland
B	172	173 [a]	146	146	178
C'	56.7	52.5 [a]	48.0	48.0	49.0
C_{44}	135	122 [a]	115	115	116
E_{coh}	4.28	4.28	4.28	4.28	4.316
$E_{\mathrm{bcc}}-E_{\mathrm{fcc}}$	−0.047	−0.050 [b]	−0.03	−0.007	−0.054
E^f_{vac}	2.04	2.0±0.2 [c]	1.63	1.56	1.70
$E^{\mathrm{SD}}_{\mathrm{vac}}$	2.91	2.91±0.04 [d]	2.32	2.29	2.48
$E^f_{\langle 110\rangle}$	7.72	3-12 [e]	3.66	4.11	4.87
$E^f_{\langle 110\rangle}-E^f_{\langle 111\rangle}$	−0.23	−0.30 [f]	+0.12	−0.19	−0.13
α ($T=300$ K)	12.8	11.7 [g]	5.8	3.4	7.4
α ($T=600$ K)	14.2	15.8 [g]	7.9	4.9	7.2

[a]Reference 32.
[b]Reference 33.
[c]Reference 34.
[d]References 35, 36.
[e]References 37, 38.
[f]Reference 38.
[g]Reference 39.

TABLE V. Properties of paramagnetic Cr calculated with the potential here presented. Comparison is made with experimental data for Cr in AFM and PM states, as well as values calculated using the potential of Farkas (Ref. 20). PM elastic constants were obtained by extrapolation to 0 K of high temperature data (Ref. 27). The paramagnetic thermal expansion coefficient at $T=300$ K refers to measurements on Cr–5V (Ref. 29).

Cr property	This work	Expt. (AFM)	Expt. (PM)	Farkas
B	207	195[a]	207[a]	148
C'	153	153[a]	155[a]	42.5
C_{44}	105	104[a]	105[a]	···
E_{coh}	4.10	4.10	4.10	4.10
$E_{\mathrm{bcc}}-E_{\mathrm{fcc}}$	−0.025	···	···	−0.053
E^f_{vac}	2.14	···	2.0±0.2[b]	1.12
$E^{\mathrm{SD}}_{\mathrm{vac}}$	2.93	···	2.95[c]	2.30
$E^f_{\langle 110\rangle}$	5.16	···	···	3.03
$E^f_{\langle 110\rangle}$-$E^f_{\langle 111\rangle}$	−0.62	···	···	0.19
α ($T=300$ K)	7.5	4.4[d]	7.9[d]	5.2
α ($T=600$ K)	9.8	···	9.6[d]	9.5

[a]Reference 27.
[b]Reference 44.
[c]Reference 45.
[d]Reference 29.

TABLE VI. Comparison of Fe-Cr mixing enthalpy obtained with the potentials here presented, the Exact Muffin Tin Orbital calculation of Olsson *et al.* (Ref. 31), and values calculated using the potential of Farkas *et al.* (Ref. 20).

Property	Data	Fe-5Cr	Fe-20Cr
H^f_{FeCr} (meV)	This work	−0.04	+45
	EMTO	−0.05	+45
	Farkas	+24	+86

Wollenberger arrives at a formation energy $E^f_F = 6.6$ eV for a Frenkel pair in electron irradiated α-Fe, and $E^f_F = 13.6$ eV for a neutron irradiated sample.[41] Subtracting a vacancy formation energy of 2.0 eV would then give $E^f_{\langle 110\rangle} = 4.6$ eV in the former case, and 11.6 eV in the latter. The uncertainty of these values is obviously large, since just by assuming $\rho_F = 0.20\ \mathrm{m}\Omega \times \mathrm{cm}$, one could obtain $E^f_{\langle 110\rangle} = 7.7$ eV for the neutron irradiated sample. Note that results from the electron irradiation not necessarily are more accurate, since experimental boundary conditions are more difficult to control in stages I_A to I_C (absent in neutron irradiation) than in stage I_D.

The SIA formation energy in iron have recently been calculated with the *ab initio* package VASP as $E^f_{\langle 110\rangle} \simeq 3.4$ eV.[46] This result is compatible with data from electron irradiations. However, since the calculation did not take into account possible effects of noncollinear magnetism, the discrepancy with data from neutron irradiated samples remains an open question. As will be seen later, the magnitude of the interstitial formation energy has a significant impact on defect recombination in recoil cascades, and we will argue that a high value is consistent with defect distributions actually observed.

Concerning the properties of chromium predicted by the potential here presented, we emphasize that the fit was made to elastic constants of *paramagnetic* chromium, extrapolated to 0 K. Hence we are able to retain a positive Cauchy pressure at all temperatures. The relaxed vacancy formation energy is compatible with experimental data, in contrast to the prediction of the potential by Farkas *et al.*,[20] for which an apparently incorrectly quoted value of E^f_{vac} has been used in the fit. We further note that the activation energy for vacancy diffusion predicted by the potential is in excellent agreement with measured data.[45]

As seen in Table VI, the alloy potentials well reproduce the mixing enthalpies of Fe-5Cr and Fe-20Cr calculated with the EMTO method. The heat of mixing obtained with Farkas' potential should be considered to represent the paramagnetic state of the alloy, and is hence not applicable for MD or KMC simulations below the Curie temperature.

Table VII displays formation and binding energies of a single mixed $\langle 110\rangle$ Fe-Cr dumbbell in an iron matrix. We find that the mixed $\langle 110\rangle$ Fe-Cr dumbbell is more stable than the $\langle 110\rangle$ Fe-Fe dumbbell in the case of local Cr concentrations less than 20%. The Cr–Cr dumbbell is even more stable, with a binding energy exceeding 0.3 eV. Hence one may expect that Cr will tend to accumulate in defect structures created in collision cascades.

TABLE VII. Formation and binding energies of a single mixed $\langle 110\rangle$ Fe-Cr dumbbell in an iron matrix with lattice parameter $a_0 = 2.860$ Å. Predictions of the alloy potentials are compared to VASP *ab initio* data (Ref. 47) and values calculated with Farkas' potential (Ref. 20). $-E^b_{\langle 110\rangle} = E^{\mathrm{Cr}}_{\langle 110\rangle} - E^{\mathrm{Fe}}_{\langle 110\rangle} - E^s_{\mathrm{Cr}}$ is calculated relative to the energy of an Fe-Fe dumbbell, subtracting the substitution energy E^s_{Cr} of a single Cr atom.

Property	$E^f_{\langle 110\rangle}$	E^s_{Cr}	$E^b_{\langle 110\rangle}$	$E^f_{\langle 110\rangle} - E^f_{\langle 111\rangle}$
Fe-5Cr	7.63	+0.18	+0.27	−0.03
Fe-20Cr	8.19	+0.46	−0.01	−0.20
VASP	3.06	−0.35	−0.00	+0.36
Farkas	4.31	+0.70	+0.05	+0.07

The sparse experimental data for the elastic constants of the alloy are unfortunately not fully consistent.[30,48] Below the solubility limit of Cr though, there is a clear tendency for a decrease in bulk modulus, which is supported by *ab initio* calculations. The range of the Fe-5Cr potential was therefore enlarged, in order to obtain a smaller bulk modulus. This procedure must however be considered as arbitrary, and better experimental data for the alloy, including thermal expansion, is of necessity to enable construction of fully consistent mixed pair potentials.

Due to the nonmonotonous behavior of the bulk modulus and the formation energy, a potential for a given Cr concentration can in general not be used for predicting alloy properties at a different concentration. Proper simulation of nonequilibrium behavior of the alloy would require use of different potentials for different local concentrations of chromium.

IV. APPLICATION OF THE Fe-Cr POTENTIAL IN SIMULATION OF THERMAL AGEING

It is well known that precipitation of Cr occurs under thermal aging at $T < 900$ K in FeCr alloys with Cr content ranging from 10% to 90%.[3,5] The formation of the so-called α' phase is responsible for hardening of the binary alloy.[49,50] The magnitude of the miscibility gap for low Cr concentrations could be theoretically explained only recently, when *ab initio* calculations showed that the mixing enthalpy of Fe-Cr is negative for the *ferromagnetic* state of the random alloy, if the Cr concentration is below 6%.[31] Above this limit, the formation energy is positive, providing a driving force for phase separation. In order to obtain the temperature dependence of the solubility, one needs to perform molecular dynamics, or rather kinetic Monte Carlo (KMC) simulations. We have performed such simulations of thermal aging at a range of temperatures, using several different techniques implemented in the DYMOKA code, developed by Electricite de France (EDF) and University of Lille.[51]

The out-of-pile process of segregation is assumed to be driven purely by vacancy assisted migration. According to classical diffusion theory, the frequency for a lattice atom to exchange lattice position with a neighboring vacancy is

$$\Gamma(T) = \nu C_{\mathrm{vac}}(T) e^{-(E_m/k_B T)}, \tag{11}$$

where ν is the attempt frequency of the jump and C_{vac} is the equilibrium concentration of vacancies. The vacancy concentration as function of temperature is given by

$$C_{\mathrm{vac}}(T) = e^{-(G_f/k_B T)}. \tag{12}$$

Here, $G_f = E^f_{\mathrm{vac}} - TS^f_{\mathrm{vac}}$ is the Gibbs energy of vacancy *formation*. The entropy of formation may be calculated from the following formula:[52]

$$S^f_{\mathrm{vac}} = k_{\mathrm{B}} \left(\sum_n^{3(N-1)} \ln \omega_n^{\mathrm{vac}} - \frac{(N-1)}{N} \sum_n^{3N} \ln \omega_n^{\mathrm{bulk}} \right), \tag{13}$$

where ω_n are eigen frequencies of the force-constant matrices with an without a vacancy in the system, respectively. MD simulations using our potential for ferromagnetic iron gives $S^f_{\mathrm{vac}} = 1.78\ k_B$ for a relaxed system of $N = 432$ atoms.

Similarly, the attempt frequency ν may be calculated from[53]

$$\nu = \frac{k_B}{2\pi} \frac{\prod_{n=1}^{3N} \omega_n^{\mathrm{vac}}}{\prod_{n=1}^{3N-1} \omega_n^{\mathrm{TST}}}, \tag{14}$$

where ω^{TST} are the eigenfrequencies evaluated at the transition state of the vacancy jump. For the present potential we obtain $\nu = 9.15 \times 10^{13}\ \mathrm{s}^{-1}$ which gives us a prefactor for self-diffusion in ferromagnetic iron: $D_0 = 2.13 \times 10^{-5}\ \mathrm{m}^2/\mathrm{s}$. This value, valid in the harmonic approximation, is very close to the one observed in experiments.[36]

In general, the probability of all possible vacancy jumps in an alloy (8 first nearest neighbors in a bcc structure) should be computed for every Monte Carlo step, selecting one of them to be performed, weighted with that probability. Time is then introduced as the inverse of the system averaged jump frequencies. In our case, the vacancy assisted migration energy for Fe and Cr atoms are close to each other; 0.87 eV and 0.84 eV, respectively. We hence make a concentration weighted average for our system and calculate an average time step as

$$\Delta\tau = \frac{1}{8\Gamma(T)}. \tag{15}$$

We performed simulations of vacancy migration assuming a single vacancy in a box with 16 000 atoms. It was checked that the rate of energy loss in the Fe-20Cr alloy did not change significantly when increasing the box size.

In order to arrive at a fully segregated final state, we used a Metropolis Monte Carlo algorithm, together with the vacancy KMC. The metropolis algorithm exchanges all atoms of differing type if it is energetically favorable. If an exchange increases the energy it is accepted with a weight $\exp(-E/kT)$, where E is the potential energy of the system. The Metropolis MC method is much faster, but provides no explicit time scale. However, it was found that a time step could be assigned to each Metropolis MC step by fitting energy losses to the explicit vacancy KMC simulation.

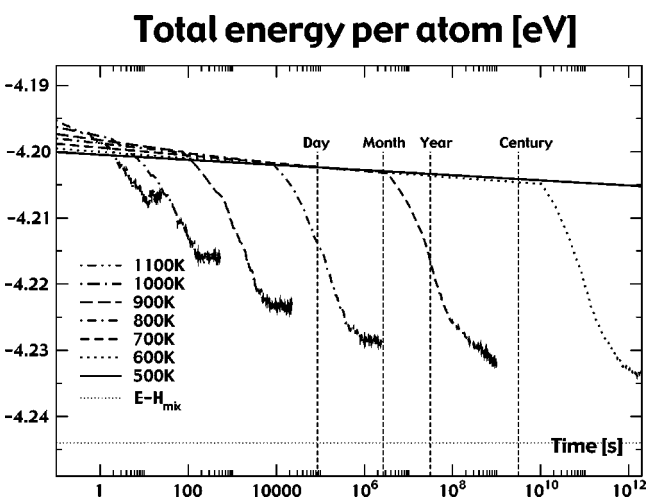

FIG. 2. Total energy of an initially random Fe-20Cr alloy, as a function of time and temperature.

In Fig. 2, the total energy of an initially random Fe-20Cr alloy is plotted as function of time and temperature. Since the mixing enthalpy of the random alloy is positive, a loss in energy is a sign of segregation. For infinite segregation, the energy loss would equal the formation energy $\Delta H^f_{\mathrm{Fe\text{-}20Cr}} = 45$ meV. In a finite box, however, there will always remain a surface to bulk factor. The surface atoms of a Cr cluster will all have Fe neighbors and thus a higher energy. In our most segregated case ($T = 500$ K) we arrive at 84% of the mixing enthalpy. This may be understood from the fact that a single Cr cluster of spherical shape in our simulation box has a surface to bulk ratio of Cr atoms equal to about 30%. On the cluster surface, half of the neighbors to Cr atoms are Fe atoms, and hence the surface energy of final Cr cluster provides the missing 16%.

We note that for 700 K, the time needed to obtain a significant energy loss is of the order of months, which is consistent with the experimental time threshold for observation of hardening in Fe-45Cr alloys aged at 673 K.[50] For 800 K segregation occurs in a matter of days, while for 900 K, the energy loss saturates within a few hours, before complete phase separation has taken place. At 1000 K, less than half the energy loss is achieved, which corresponds to a limited ordering of the system, without actual phase separation.

The process of segregation is illustrated in Fig. 3, where the distribution of Cr atoms is shown before and after ageing during 30 years at 700 K. This simulation was done with an initial Cr content equal to 12%, using the Fe-20Cr potential.

The final Cr-precipitate appearing during the simulation is free of Fe atoms, due to the fact that our potential incorrectly predicts a positive mixing enthalpy even for Cr concentrations in the vicinity of 90%.

In order to quantify the temperature dependence of the phase separation, we define the degree of segregation ξ as

$$\xi = \frac{1}{\xi_{\max}} \frac{N^{\mathrm{Emb}}_{\mathrm{Cr}}}{N^{\mathrm{Tot}}_{\mathrm{Cr}}}. \tag{16}$$

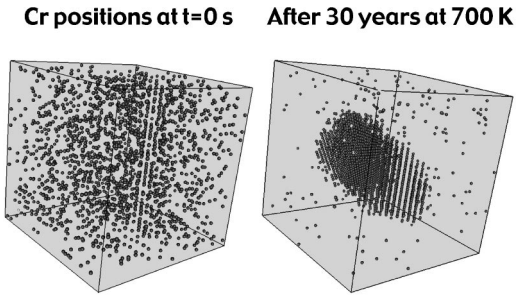

FIG. 3. Distribution of Cr atoms in a box with 16 000 atoms, before and after thermal aging at 700 K. A crystal clear segregation is observed, with formation of a single cluster.

Here, $N_{\mathrm{Cr}}^{\mathrm{Tot}}$ is the number of Cr atoms in the system, $N_{\mathrm{Cr}}^{\mathrm{Emb}}$ is the number of Cr atoms that only have Cr first nearest neighbors, and ξ_{max} is the theoretical maximum number of Cr atoms that may have Cr first nearest neighbors, accounting for the surface layer of a spherical cluster.

The degree of segregation produced by the Fe-20Cr potential after the energy loss has reached its asymptotic value is shown in Fig. 4. If an arbitrary limit of $\xi > 0.5$ is set to distinguish the α' phase from α, we find that this corresponds to $T < 900$ K. Considering that the range of temperature where the phase transition takes place is uncertain, quoted as 750 ± 125 K in Ref. 7, our results may be considered to be in reasonable agreement with the phase diagram.

Performing the same type of simulations using the potential fitted to the mixing enthalpy of Fe-5Cr, no significant energy loss is found at any temperature, which means that the alloy remains random. We may thus conclude that our potentials reproduce the out-of pile state of ferromagnetic Fe-Cr as function of temperature and time at Cr concentrations of 0%, 5%, and 20%.

It is important to note that in reality, the driving force for the decomposition would be lost when the local concentration of Cr becomes too high or too low. Hence, in order to obtain the physically observed final states with an iron content in the α' precipitates ranging from 10% to 20%, we would have to switch potentials during the simulation according to the local density of Cr, a feature not yet implemented in the codes we have used. Therefore the size of the clusters we observe at infinite times cannot be expected to agree with the measured size distribution, being of the order of 2–4 nm.[50]

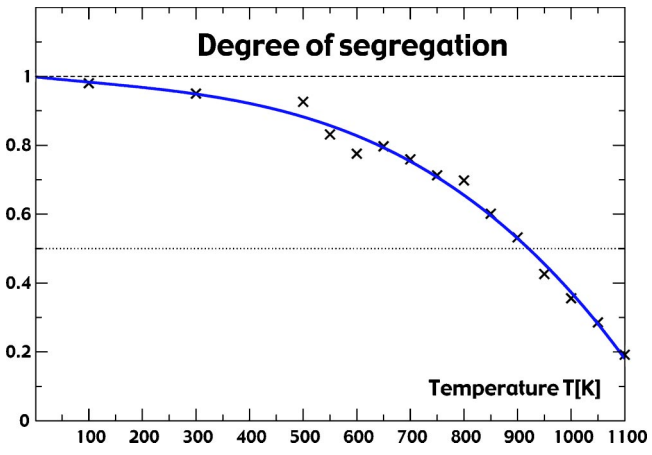

FIG. 4. (Color online) Degree of segregation ξ as a function of temperature. The line is a cubic fit to asymptotic averages obtained with the Metropolis Monte Carlo procedure.

TABLE VIII. Average number of surviving Frenkel pairs as function of recoil damage energy. The quoted uncertainty corresponds to one standard deviation.

E_{dam}	5 keV	10 keV	20 keV
Fe	7.4 ± 0.7	13.4 ± 0.9	27.0 ± 1.0
Fe-5Cr	8.9 ± 0.7	14.0 ± 0.8	28.7 ± 1.6
Fe-20Cr	8.5 ± 0.6	13.6 ± 0.7	27.0 ± 1.3

V. APPLICATION OF THE Fe-Cr POTENTIAL IN CASCADE SIMULATIONS

The potentials here presented were applied in molecular dynamics simulations of collision cascades initiated by recoils having energies up to 20 keV. Periodic boundary conditions were used, and the sizes of the MD boxes were adjusted to make sure that the cascade did not interact with its periodic image. For 10 keV cascades, it was found that 128 000 atoms ($40 \times 40 \times 40$ lattice units) was sufficient for recoils in the $\langle 135 \rangle$ direction, while 250 000 atoms had to be used when launching in the $\langle 111 \rangle$ direction. The initial atom velocities were sampled from a Maxwellian distribution for a particular temperature, set to $T = 100$ K in the present study. The block is equilibrated for about a picosecond before launching an energetic recoil in the central region. The time step was varied from 0.02 fs (when the recoil is generated) up to 0.5 fs at the end of the simulation period (10 ps). The first thing to be noted is that the new potentials predict a much smaller number of surviving defects than potentials found in the literature.[11,54] This is a direct result of the higher interstitial formation energy, leading to larger probability for recombination of Frenkel pairs during cooling down of the cascade. Table VIII shows the average number of surviving defects in Fe and Fe-20Cr, for a set of representative recoil energies in the $\langle 135 \rangle$ direction.

As seen the difference between the alloy and pure iron is statistically insignificant. For recoil energies between 10 and 20 keV, we arrive at a cascade efficiency of 0.135 ± 0.005 NRT, which may be compared to a value of 0.3 NRT in pure Fe obtained at $T = 100$ K with a Finnis-Sinclair potential yielding an SIA formation energy of 4.9 eV.[54]

The main impact of introducing chromium is found in the relative population of the elements in the defects produced by the cascade. In Fe-5Cr, where the Fe-Cr dumbbell is more stable than the pure Fe-Fe dumbbell, the fraction of chromium atoms in the surviving interstitial defects is as large as 19%, fairly independent of recoil energy. The mixed dumbbells are less mobile than pure Fe interstitials, and will thus act as obstacles for migration of Fe interstitial clusters. In Fe-20Cr, where the mixed Fe-Cr and pure Fe-Fe dumbbells have about the same energy, chromium atoms constitute roughly 30% of the interstitial atoms.

VI. CONCLUSIONS

The set of EAM potentials for Fe-Cr alloys implemented in the present work yield activation energies for vacancy migration in the pure elements that are in very good agreement with experimental data. The predicted SIA formation energies arising from fitting to thermal expansion coefficients are higher than values obtained by other authors using both EAM and *ab initio* methods. While electron irradiation data seems to support lower numbers, the stored energy release measured in neutron irradiated samples is compatible with our results. Our potentials further correctly predict the $\langle 110 \rangle$ interstitial to be the stable form in both the pure elements as well as in the alloy.

Applied to simulation of thermal aging, there is no sign of precipitation taking place when using the potential fitted to the negative formation energy previously calculated for ferromagnetic Fe-5Cr. KMC simulations using the potential fitted to the mixing enthalpy of Fe-20Cr yield formation of Cr clusters on a time and temperature scale that is in good agreement with measurements of hardening in high Cr binary alloys.

We predict that the $\langle 110 \rangle$ Fe-Cr and Cr–Cr dumbbells are more stable than the corresponding defect in pure iron. Consequently, Cr will tend to end up in defect structures forming during cooling down of recoil cascades, and we register that 19% of the interstitial atoms in Fe-5Cr are chromium atoms.

The total number of defects surviving after recoil cascades is smaller than predicted by Fe potentials from the literature. This fact is directly related to the higher SIA formation energy. For damage energies between 10 and 20 keV, we obtain a cascade efficiency of 0.135 ± 0.005 NRT at $T = 100$ K, which in part may explain the long standing mystery of the small number of freely migrating defects observed in experiments.[55]

ACKNOWLEDGMENTS

The authors would like to thank I. Abrikosov, A. Almazousi, L. Malerba, B. Singh, D. Bacon, and Y. Osetski for inspiring discussions. This work was supported in part by the Svensk Kärnbränslehantering AB (J.W.), EU 5th FP project SPIRE (J.W., R.C., and V.P.), STINT, EURATOM, and the Swedish Council (P.O.), and Svenskt Kärntekniskt Centrum (C.L.).

[1] E. Little and D. Stow, J. Nucl. Mater. **87**, 25 (1979).
[2] F. Garner, M. Toloczko, and B. Sencer, J. Nucl. Mater. **276**, 123 (2000).
[3] R. Fischer, E. Dulis, and K. Carroll, Trans. AIME **197**, 690 (1953).
[4] E. Little and L. Stoter, in *Effect of Radiation on Materials, ASTM STP* (1982), Vol. 782, p. 207.
[5] H. Kuwano, Trans. JIM **26**, 473 (1985).
[6] M. Miller, J. Hyde, A. Cerezo, and G. Smith, Appl. Surf. Sci. **87/88**, 323 (1995).
[7] M. Mathon, Y. Carlan, G. Geoffrey, X. Averty, A. Alamo, and C. de Novion, J. Nucl. Mater. **312**, 236 (2003).
[8] R. Johnson, Phys. Rev. B **39**, 12554 (1985).
[9] A. Voter, in *Intermetallic Compounds, Principles*, edited by J.H. Westbrook and R.L. Fleischer (Wiley, New York, 1995), Vol. 1.
[10] M. Finnis and J. Sinclair, Philos. Mag. A **50**, 45 (1984).
[11] A. Calder and D. Bacon, J. Nucl. Mater. **207**, 25 (1993).
[12] G. Ackland, D. Bacon, A. Calder, and T. Harry, Philos. Mag. A **75**, 713 (1997).
[13] M. Daw and M. Baskes, Phys. Rev. B **29**, 6443 (1984).
[14] R. Pasianot, D. Farkas, and E. Savino, Phys. Rev. B **43**, 6952 (1991); **47**, 4149(E) (1993).
[15] G. Simonelli, R. Pasianot, and E. Savino, Mater. Res. Soc. Symp. Proc. **291**, 567 (1993).
[16] G. Simonelli, R. Pasianot, and E. Savino, Phys. Rev. B **50**, 727 (1994).
[17] G. Simonelli, R. Pasianot, and E. Savino, Phys. Status Solidi **217**, 747 (2000).
[18] O. Yifang, Z. Bangwei, L. Shuzhi, and J. Zhanpeng, Z. Phys. B: Condens. Matter **101**, 161 (1996).
[19] T. Konishi, K. Ohsawa, H. Abe, and E. Kuramoto, Comput. Mater. Sci. **14**, 108 (1999).
[20] D. Farkas, C. Schon, M. de Lima, and H. Goldstein, Acta Mater. **44**, 409 (1996).
[21] J. Rose, J. Smith, and J. Ferrante, Phys. Rev. B **28**, 1835 (1983).
[22] J. Adams and S. Foiles, Phys. Rev. B **41**, 3316 (1990).
[23] P. Legrand, Ph.D. thesis, University of Paris, 1993.
[24] G. Evangelakis, J. Rizos, I. Lagaris, and I. Demetropoulos, MERLIN, a portable system for multidimensional minimization, University of Ioannina, 1986.
[25] J. Rifkin, XMD, Center for Materials Simulation, University of Connecticut, 1999.
[26] J. Biersack and J. Siegler, J. Nucl. Inst. Methods **141**, 93 (1982).
[27] K. Katahara, M. Nimalendran, M. Manghnani, and E. Fischer, J. Phys. F: Met. Phys. **9**, 2167 (1979).
[28] S. Burke, R. Cywinski, J. Davis, and B. Rainford, J. Phys. F: Met. Phys. **13**, 451 (1983).
[29] G. White, R. Roberts, and E. Fawcett, J. Phys. F: Met. Phys. **16**, 449 (1986).
[30] G. Speich, A. Schwoeble, and W. Leslie, Metall. Trans. **3**, 2031 (1972).
[31] P. Olsson, I. Abrikosov, L. Vitos, and J. Wallenius, J. Nucl. Mater. **321**, 84 (2003).
[32] J. Rayne and B. Chandrasekar, Phys. Rev. **122**, 1714 (1961).
[33] W. Bendick and W. Pepperhof, Acta Metall. **30**, 679 (1982).
[34] L.D. Schepper, D. Segers, L. Dorikens-Vanpraet, M. Dorikens, G. Knuyt, L. Stals, and P. Moser, Phys. Rev. B **27**, 5257 (1983).
[35] M. Lübbehusen and H. Mehrer, Acta Metall. Mater. **38**, 283 (1990).
[36] A. Seeger, Phys. Status Solidi A **167**, 289 (1998).
[37] P. Moser, Mem. Sci. Rev. Metall. **63**, 431 (1966).
[38] H. Bilger, V. Hivert, J. Verdone, J. Leveque, and J. Soulie, in *International Conference on Vacancies and Interstitials in Metals* (Kernforshungsanlage Jülich, Germany, 1968), p. 751.

[39] F. Nix and D. MacNair, Phys. Rev. **60**, 597 (1941).
[40] H. Schaefer, K. Maier, M. Weller, D. Herlach, A. Seeger, and J. Diehl, Scr. Metall. **11**, 803 (1977).
[41] H. Wollenberger, in *Physical Metallurgy*, edited by R. Cahn and P. Haasen (North–Holland, Amsterdam, 1996), Vol. 2.
[42] P. Vadja, Rev. Mod. Phys. **49**, 481 (1977).
[43] P. Erhart, Mater. Res. Soc. Symp. Proc. **41**, 13 (1985).
[44] G. Loper, L. Smedskjaer, M. Chason, and R. Siegel, in *Positron Annihilation*, edited by P. Jain, R. Singru, and K. Gopinathan (World Scientific, Singapore, 1985), p. 461.
[45] H. Schultz, Mater. Sci. Eng., A **141**, 149 (1991).
[46] C. Domain and C. Becquart, Phys. Rev. B **65**, 024103 (2002).
[47] C. Domain (private communication, 2002), quoted in Olsson *et al.*, SCK-CEN-BLG-950.
[48] H. Maxumoto and M. Kikuchi, Trans. JIM **12**, 90 (1975).
[49] S. Brenner, M. Miller, and W. Soffa, Scr. Metall. **16**, 831 (1982).
[50] J. Hyde, M. Miller, A. Cerezo, and G. Smith, Appl. Surf. Sci. **87/88**, 311 (1995).
[51] C. Domain and C. Becquart, *DYMOKA User's Guide*, 6th ed. (2002).
[52] G. Grimvall, *Thermodynamic Properties of Materials* (Elsevier, New York, 1999).
[53] G. Vineyard, J. Phys. Chem. Solids **3**, 121 (1957).
[54] R. Stoller, G. Odette, and B. Wirth, J. Nucl. Mater. **251**, 49 (1997).
[55] L. Rehn, J. Nucl. Mater. **174**, 144 (1990).